Bioelectrochemistry 154 (2023) 108553

Contents lists available at ScienceDirect

Bioelectrochemistry

journal homepage: www.journals.elsevier.com/bioelectrochemistry

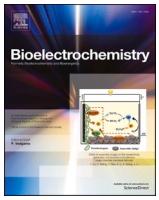

Electrochemical miRNA-34a-based biosensor for the diagnosis of Alzheimer's disease

Raquel L. Pereira [a,b,c,d,e], Daniela Oliveira [a,b,c], Ana P. Pêgo [d,e,f], Sofia D. Santos [d,e], Felismina T.C. Moreira [a,b,c,*]

[a] CIETI-LabRISE, School of Engineering, Polytechnic Institute, 4249-015 Porto, Portugal
[b] CEB, Centre of Biological Engineering, Minho University, 4710-057 Braga, Portugal
[c] LABBELS – Associate Laboratory, 4710-057 Braga/Guimarães, Portugal
[d] i3S – Instituto de Investigação e Inovação em Saúde, Universidade do Porto, Rua Alfredo Allen, 208, 4200-135 Porto, Portugal
[e] INEB – Instituto de Engenharia Biomédica, Universidade do Porto, Porto, Portugal
[f] ICBAS – Instituto de Ciências Biomédicas Abel Salazar, Universidade do Porto, Porto, Portugal

ARTICLE INFO

Keywords:
miRNA-34a
Electrochemical biosensor
Alzheimer's disease
Gold nanoparticles
Carbon screen-printed electrodes

ABSTRACT

Alzheimer's disease (AD) is the most common dementia type and a leading cause of death and disability in the elderly. Diagnosis is expensive and invasive, urging the development of new, affordable, and less invasive diagnostic tools. The identification of changes in the expression of non-coding RNAs prompts the development of diagnostic tools to detect disease-specific blood biomarkers. Building on this idea, this work reports a novel electrochemical microRNA (miRNA) biosensor for the diagnosis of AD, based on carbon screen-printed electrodes (C-SPEs) modified with two gold nanostructures and a complementary anti-miR-34a oligonucleotide probe. This biosensor showed good target affinity, reflected on a 100 pM to 1 μM linearity range and a limit of detection (LOD) of 39 pM in buffer and 94 aM in serum. Moreover, the biosensor's response was not affected by serum compounds, indicating selectivity for miR-34a. The biosensor also detected miR-34a in the cell culture medium of a common AD model, stimulated with a neurotoxin to increase miR-34a secretion. Overall, the proposed biosensor makes a solid case for the introduction of a novel, inexpensive, and minimally invasive tool for the early diagnosis of AD, based on the detection of a circulating miRNA overexpressed in this pathology.

1. Introduction

AD is a multifactorial age-related disease [1] characterized by progressive neurodegeneration [2]. It accounts for 60 to 80% of all dementia cases [3] and is an important cause of death and disability in the elderly [4]. In the absence of effective curative and preventive treatments [5], early diagnosis is the most important tool for improving patient outcomes [6]. Given the invasive and expensive diagnostic methods available, the identification of new, low-cost, minimally invasive biomarkers for AD is paramount [7,8].

miRNAs are small non-coding RNAs, about 18–24 nucleotides in length, that regulate mRNA translation [9]. They are involved in key biological processes, including apoptosis, proliferation, and differentiation [10]. In the nervous system, miRNAs are also associated with neuronal patterning, synaptogenesis, neuronal plasticity, and neurodegeneration [11,12]. Due to their prominent role in fine-tuning gene expression [13], miRNAs have been associated with various pathological conditions [14] and have been described as promising biomarkers for various diseases [15]. miRNAs are present in various fluids, including plasma, serum, and cerebrospinal fluid (CSF) [16], usually in a vesicle-independent/free-floating form, which facilitates their quantification and use as biomarkers for early disease diagnosis [12,17]. Moreover, miRNAs are resistant to RNAse degradation and remain stable after prolonged storage, high temperatures, extreme pH conditions, or multiple freeze–thaw cycles [9].

miR-34a has been linked to oncogenesis and malignancies in the past [18]. However, recent evidence suggests a link between miR-34a and brain neurophysiology/pathology [19], particularly in AD, making it a promising biomarker for this disease. First, miR-34a was found to be upregulated in the brain and CSF of AD patients [20] and this

* Corresponding author at: BioMark Sensor Research/ISEP, School of Engineering of the Polytechnic School of Porto, R. Dr. António Bernardino de Almeida, 431, 4249-015 Porto, Portugal.
E-mail address: ftm@isep.ipp (F.T.C. Moreira).

https://doi.org/10.1016/j.bioelechem.2023.108553
Received 24 July 2023; Received in revised form 25 August 2023; Accepted 26 August 2023
Available online 28 August 2023

upregulation positively correlated with the severity of AD pathology [9]. Second, it was observed that the expression of miR-34a was dysregulated in blood and increased in CSF of AD patients [11]. Third, overexpression of miR-34a in mice brains resulted in cognitive impairment, tau hyperphosphorylation, and accumulation of intracellular Aβ [21]. Fourth, human SH-SY5Y cell models showed that the downregulation of miR-34a decreased the amount of active caspase-3 (an effector caspase involved in late-stage apoptosis), strengthening the link between aberrant miR-34a expression, apoptosis, and neuroprotection [22].

Typical detection of miRNA is performed by Northern blotting, quantitative reverse transcription (RT-qPCR) or microarray profiling, all of which are expensive, complicated and time-consuming methods [23]–[25]. For detection in cell-free body fluids, biosensors are a tempting alternative because they are faster, simpler, and require smaller sample volumes than other techniques [12]. In addition, biosensors are portable, sensitive, inexpensive, suitable for a wide range of concentrations, and associated with low limits of detection (LODs) – achieving femto-picomolar LODs [26]. The low-cost aspect of electrochemical biosensors becomes even more apparent when using screen-printed electrodes, especially C-SPEs, which can be mass-produced quite inexpensively [27].

Recently, the incorporation of proteins or nucleic acids into biosensor designs has attracted considerable attention because it can improve the sensitivity, response, and recovery time of biosensors [28,29]. Similarly, nanomaterials have opened new opportunities in the field of biosensor fabrication [30]. For example, nanoscale electrode patterning has been shown to improve biosensor performance by either enhancing the electrochemical signal, facilitating interfacial target detection, or enabling precise immobilization of functional components [31].

Small metallic particles such as gold nanoparticles (AuNPs) exhibit high surface electron mobility, which not only enhances their conductivity but also enables plasmonic properties and behavior as delocalized redox molecules [32,33]. These unique size-dependent properties make AuNPs an excellent platform for biosensor fabrication because they amplify the generated electrochemical signal [31,34–36]. This signal amplification also results from the increase in surface area and surface curvature when the electrode is patterned with AuNPs. The larger surface area increases the number of probes immobilized on the surface of the biosensor [27], while the curved surface reduces the steric hindrance of the interactions between the target analyte and the immobilized probe [37]. AuNPs are also widely used for biosensor fabrication because they are very stable, easy to fabricate, and can withstand a wide range of electrochemical potentials [30]. In addition, AuNPs react well with organosulfur compounds via Au-S covalent bonds and allow the formation of stable self-assembled monolayers [38].

Previously, *Serrano et al.* used electrodeposited AuNPs to modify C-SPEs for the detection of miR-21-5p [12]. Similarly, some authors have developed hybridization-based biosensors for the detection of miR-34a, which are summarized in **Table S1**. Overall, all reported examples were selective for miR-34a, showing a linear response within the range of tenths of μg mL^{-1} and an LOD of 20–300 nM miR-34a. Inspired by these authors, this work reports for the first time in the literature the modification of C-SPEs with AuNPs and a complementary anti-miR-34a oligonucleotide probe for the diagnosis of AD. The designed biosensor was sensitive to the target miR-34a, even in the presence of serum or biological samples. It also showed a linear response comparable to existing miR-34a biosensor platforms, while obtaining a lower LOD. By combining the specificity of AuNPs and miRNA sequence with the affordability of C-SPEs, the developed biosensor established itself as a great proof of concept of a new, low-cost, minimally invasive diagnostic tool for AD.

2. Experimental section

2.1. Reagents and solutions

The chemicals used were all analytical grade. Solutions were prepared with ultrapure water (obtained from a Milli-Q water purification system).

Potassium hexacyanoferrate II-3-hydrate ($K_4[Fe(CN)_6]$), magnesium chloride 6-hydrate ($MgCl_2.6\ H_2O$), and potassium hexacyanoferrate III ($K_3[Fe(CN)_6]$) were obtained from Riedel de Haën; disodium hydrogen phosphate ($Na_2HPO_4{\cdot}2H_2O$) from Carlo Erba; sodium dihydrogen phosphate dihydrate ($NaH_2PO_4{\cdot}2H_2O$) from Scharlau; L-Asparagine (Asn, $C_4H_8N_2O_3$), sulfuric acid 95–97% (H_2SO_4), 3-mercaptopropionic acid (3-MPA, $C_3H_6O_2S$), 1-ethyl-3-(3-dimethylaminopropyl)carbodiimide (EDAC), 4-(2-hydroxyethyl)-1-piperazineethanesulfonic acid (HEPES, $C_8H_{18}N_2O_4S$), ammonium chloride (NH_4Cl), and bovine serum albumin (BSA) from NZYTech; retinoic acid (RA), 6-hydroxydopamine (6-OHDA), Triton X-100, and paraformaldehyde (PFA) from Merk; N-hydroxysuccinimide (NHS) and creatinine ($C_3H_3NO_2$) from Fluka; sodium chloride (NaCl) from Normapur; hydrogen tetrachloroaurate (III) hydrate ($HAuCl_4{\cdot}xH_2O$) from Alfa Aesar; DMEM (1x) + GlutaMAX™-I (Dulbecco's Modified Eagle Medium supplemented with pyruvate and 4.5 g/L D-glucose), low-glucose DMEM (1x) + GlutaMAX™-I (Dulbecco's Modified Eagle Medium supplemented with pyruvate and 1 g L^{-1} D-glucose), and foetal bovine serum (FBS) from Gibco; gentamicin sulphate 50 mg mL^{-1} from Biowest; 4′,6-diamidino-2-phenylindole (DAPI), Flash Phalloidin™ Red 594, and mouse anti-B-tubulin III antibody from BioLegend; IgG donkey anti-mouse antibody marked with Alexa Fluor 488 from Invitrogen™; ibidi® Mounting Medium from ibidi® GmbH; trypsin-EDTA (0.25%) from Thermofisher scientific. Phosphate-buffered saline (PBS) was prepared in-house according to the laboratory's guidelines.

Oligonucleotide sequences were obtained from MeTabion. Both the anti-miR-34a and the miR-34a used for calibrations were mimetic models, of DNA nature. The anti-miR-34a has an amine 5′-end followed by poly-A spacers and its complete sequence is 5′-C6 NH_2-AAA AAA ACA ACC AGC TAA GAC ACT GCC A-3′. The miR-34a complete sequence is 5′-TGG CAG TGT CTT AGC TGG TTG T-3′. Finally, the miR-107 is of RNA nature and its complete sequence is 5′-AGC AGC AUU GUA CAG GGC UAU CA-3′.

2.2. Apparatus

Electrochemical data were obtained using PGSTAT302N, a potentiostat/galvanostat from Metrohm Autolab controlled by Nova 2.1.5 software. Metrohm DropSens C-SPEs (ref. 110) were connected to the potentiostat via a box plug from BioTid Electronical.

Scanning electron microscopic analysis (SEM) was performed using a high-resolution (Schottky) scanning electron microscope: Quanta 400 FEG ESEM /EDAX Genesis X4M.

Cell cultures were visualized at regular intervals using an Olympus CKX41 brightfield inverted microscope and a 10x objective. Immunocytochemical preparations were visualized using a Zeiss Axiovert 200 M inverted fluorescence microscope. Images were acquired using a 40x oil objective and a black-and-white camera. Images were subsequently analyzed using ImageJ (version 1.53 t).

2.3. Electrochemical assays

The electrochemical properties of the biosensors were determined using a solution of 5 mM $K_4[Fe(CN)_6]$ and 5 mM $K_3[Fe(CN)_6]$ in phosphate buffer at pH = 7.4. Cyclic voltammetry (CV) was performed with 3 consecutive CVs ranging from −0.4 to +0.7 V and a scan rate of 50 mV s^{-1}. Square-wave voltammetry (SWV) tests were performed in the range of −0.4 to +0.7 V, with a frequency of 5 Hz and an amplitude of 20 mV. Electrochemical impedance spectroscopy (EIS) was performed at open

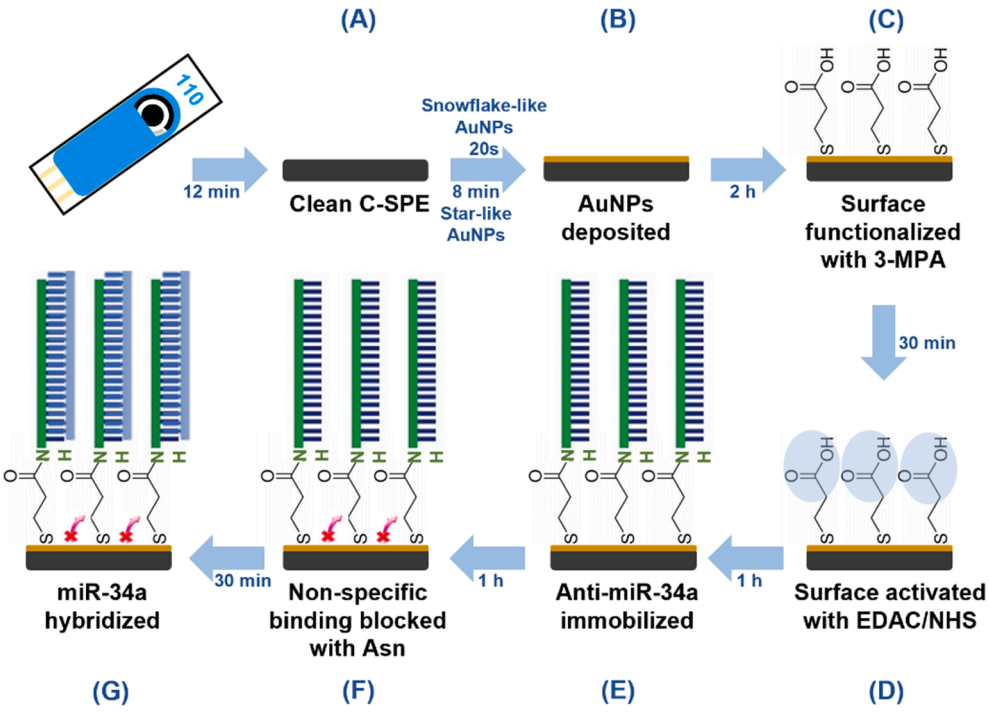

Fig. 1. Schematic representation of the biosensor's assembly and hybridization process. (A) pre-treatment of the C-SPE with H_2SO_4, (B) electrodeposition of the star- or snowflake-like AuNPs, (C) modification of the WE with 3-MPA, (D) surface activation with EDAC/NHS, (E) immobilization of the anti-miR-34a oligonucleotide probe, (F) blockage of the non-specific binding with L-asparagine (Asn) and (G) hybridization of the miR-34a target sequence.

circuit potential with a sinusoidal potential perturbation of 0.01 V amplitude and 45 frequencies in a frequency range of 0.1 to 100,000 Hz.

2.4. Modification of the commercial C-SPEs

Commercial C-SPEs (with a silver reference electrode) were modified with two different AuNP morphologies, according to *Zhao et al.* [40] or *Moreira et al.* [41]. In both cases, the electrodes were first subjected to 30 consecutive CVs (ranging from −0.2 to +1.0 V, with a scan rate of 100 mV/s) in 0.5 M H_2SO_4. Then, 10 mM $HAuCl_4$ (in 0.5 M H_2SO_4) was added to the electrodes, and star-shaped AuNPs were electrodeposited through 15 consecutive CVs (ranging from +0.6 to −0.2 V, with a scan rate of 50 mV/s). Alternatively, 100 mM $HAuCl_4$ (in 1 M NH4Cl) was added to the electrodes and snowflake-shaped AuNPs were electrodeposited by chronoamperometry (CA) by applying a potential of −0.7 V for 10 s, followed by a potential of −1.5 V for 10 s. In each case, the working electrode (WE) was modified with 10 mM 3-MPA for 2 h and its surface was activated by an EDAC/NHS reaction (12.5 mM NHS: 10 mM EDAC in 10 mM HEPES buffer) for 30 min. Finally, the WE was functionalized with 10 μM anti-microRNA-34a (previously heated to 90 °C for 5 min) for 1 h, and the non-specific binding sites were blocked with 50 mM L-asparagine (Asn) for 1 h.

2.4.1. Calibration of the biosensor

Calibration was performed in hybridization buffer and FBS. FBS was first diluted in hybridization buffer (1:100) and filtered using a 100 kDa Amicon Ultra-2 centrifugal filter unit from Millipore (2 mL sample, filtered at 8500 g, for 5 min). The biosensor was then stabilized in solvent and miR-34a solutions with increasing concentrations (0.1 nM, 1 nM, 10 nM, 100 nM, and 1 μM) were incubated for 30 min on the WE. Charge transfer resistance (R_{ct}) was extracted using Nova 2.1.5 software and calibration curves were obtained by plotting the logarithm of miR-34a concentration against the normalized value of R_{ct}.

2.4.2. Specificity/ selectivity tests

To assess the specificity/selectivity of the biosensor, its EIS response was evaluated in the presence of 900 nM creatinine,10 fM microRNA-107 or FBS (filtered and diluted as previously described). For this purpose, the biosensor was stabilized in hybridization buffer and the test solution (containing the interferent and/or 0.1 nM miR-34a) was incubated for 30 min on the WE. EIS was measured and R_{ct} was extracted using Nova 2.1.5 software.

2.5. In vitro proof of concept

2.5.1. Cell culture

SH-SY5Y cells were cultured in Non-differentiation medium (DMEM (1x) + GlutaMAX™-I, containing 15% FBS (heat-inactivated for 30 min, at 56 °C) and 0.1% gentamicin sulfate 50 mg mL^{-1}). The culture flasks were incubated in a humidified environment at 37 °C and 5% CO_2. The medium was changed regularly, and the cells were divided at approximately 80% confluence with trypsin-EDTA. Cells were regularly examined under bright field microscope to observe their morphology and health status.

2.5.2. Neuronal differentiation and stimulation of miR-34a secretion

Neuronal differentiation was performed using a protocol adapted from *Simões et al.* [42]. Briefly, cells were plated in a 96-well plate at a density of 20,000 cells/well (for differentiation) or 15,000 cells/well (as a non-differentiated control – Non_DIFF) and cultured in Non-differentiation medium. For differentiation, the medium was replaced 24 h after plating with the Differentiation medium (DMEM with low glucose, 1% FBS, 0.1% gentamicin sulfate 50 mg mL^{-1}, and 10 μM RA) - DIFF_0. To increase the expression and secretion of miR-34a into the cellular medium, the medium was replaced 4 days after plating with Differentiation medium supplemented with 50 μM or 100 μM 6-OHDA - DIFF_50 and DIFF_100. 5 days after plating (with 1 day under 6-OHDA stimulation), the medium was partially removed, and the cells were prepared for immunocytochemistry.

2.5.3. Immunocytochemistry

After the experiments in section 2.5.2., the cells were fixed by adding

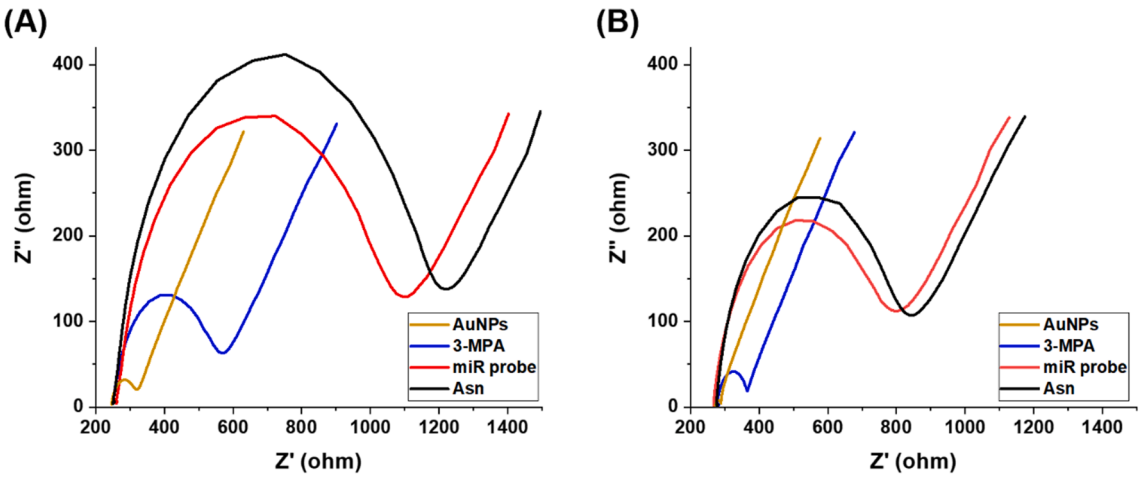

Fig. 2. Representative examples of the EIS curves obtained for the design process of the biosensors modified with (A) star-like or (B) snowflake-like AuNPs. AuNPs: gold nanoparticles; 3-MPA: 3-mercaptopropionic acid; miR probe: anti-miRNA-34a; Asn: L-asparagine. Electrochemical measurements performed in 5 mM $[Fe(CN)_6]^{3-/4-}$ in phosphate buffer, pH = 7.4.

8% PFA (in PBS) to the remaining culture media (in a 1:1 proportion) and incubating for 10 min. Afterwards, the cells were permeabilized with 0.1% Triton X-100 for 5 min and unspecific binding sites were blocked with Blocking Solution (1% BSA in PBS) for 1 h. To visualize β-tubulin III, the cells were incubated in mouse anti-β-tubulin III antibody (1:500 in Blocking Solution) for 1 h, followed by IgG Alexa 488 donkey anti-mouse antibody (1:1000 in Blocking Solution) for 1 h. To visualize the nuclei, the cells were incubated in DAPI (1:10,000 in Blocking Solution) for 10 min. To visualize F-actin, the cells were incubated in Flash Phalloidin™ Red 594 (1:40 in PBS), for 20 min. After staining, two drops of ibidi Mounting Medium were added to each well and the prepped plates were stored in PBS, in the dark, at 4 °C, until analysis.

2.5.4. Testing the biosensor in cellular media extracts

The biological samples used to test the biosensors were collected in section 2.5.2.. First, the biosensors were stabilized in Differentiation medium (1:100 in hybridization buffer), filtered using a Millipore 100 kDa Amicon Ultra-2 centrifugal filter unit (2 mL sample filtered at 8500 g for 5 min). Next, each biosensor received a media sample of one of the tested conditions - DIFF_0, DIFF_50, or DIFF_100 - filtered and diluted as previously described. Finally, the shift in R_{ct} caused by the presence of miR-34a in the samples was analyzed.

3. Results and discussion

3.1. Biosensor assembly

The biosensor's assembly process is schematized in Fig. 1 and involves six main steps: (A) C-SPE pre-treatment, (B) AuNPs electrodeposition, (C) 3-MPA surface modification, (D) EDAC/NHS surface activation, (E) oligonucleotide immobilization and, (F) non-specific binding blockage.

First, the C-SPEs were pretreated in H_2SO_4 to remove impurities and activate the surface for the deposition of AuNPs. Electrodeposition of AuNPs was performed not only to improve the conductivity of the electrodes but also to increase the surface area available for modification. Then, 3-MPA was added to WE to functionalize it with carboxyl groups and allow covalent bonding of the amine-terminated probe (by carbodiimide reaction). This reaction was further promoted with EDAC/NHS. Finally, after functionalization of WE with the anti-microRNA-34a sequence (previously linearized to favor subsequent interactions with the complementary miR-34a strands) and blocking of the non-specific binding sites with L-asparagine (Asn), hybridization with the miR-34a target sequence was promoted.

3.2. Electrochemical follow-up of the biosensor's assembly

3.2.1. Effect of the gold nanostructures on the miR-34a's binding efficiency

Representative examples of the electrodeposition results of the star- and snowflake-shaped AuNPs are shown in **Figure S.1**. Briefly, the results obtained for the two nanostructures are very similar. Both biosensors show an increase in conductivity or a decrease in R_{ct} after electrodeposition of the AuNPs, indicating successful modification of the C-SPEs. It is important to note that the results obtained for both electrodeposition processes are reproducible. At this stage, the relative standard deviation (RSD) among samples is only 3.6% for the star-like morphology and 8.5% for the snowflake-like morphology.

Fig. 2 is a representative example of the results obtained for the entire biosensor's design process. Here, the R_{ct} value increased after each modification step, indicating that the insulating layers were gradually immobilized on the surface of WE. It can be concluded that the biosensor's assembly was successful for both gold nanostructures, despite the differences in absolute R_{ct} values. Since the R_{ct} value was lower for the star-shaped AuNPs, it can also be concluded that electron transfer is favored by this nanostructure.

3.3. Analytical performance of the biosensor

3.3.1. Gold nanostructure selection

The effect of the AuNP's structure on the analytical performance of the biosensors was evaluated using calibration curves with different miR-34a standards. After stabilization in buffer, the miR-34a standards were incubated sequentially on the WE, from lowest (0.1 nM) to highest concentration (1000 nM). The electrochemical properties were measured in between standards using a $[Fe(CN)_6]^{3-/4-}$ redox solution, and the successful hybridization of miR-34a was demonstrated by the continuous increase of R_{ct}.

Fig. 3 shows the EIS spectra, calibration curves, and SEM images of the two biosensor types. The EIS analysis in Fig. 3**A** shows an increase in R_{ct} after each incubation. This indicates progressive binding of miR-34a to the surface of the WE and suggests successful hybridization of miR-34a to the biosensors of both morphologies. However, R_{ct} variation is less regular and generally less pronounced on the biosensors modified by CA, which may indicate that the snowflake-like AuNPs are less favorable for the hybridization process.

Regarding the calibration curves on Fig. 3**B**, the coefficient of determination (R^2) is similar for both morphologies. However, the

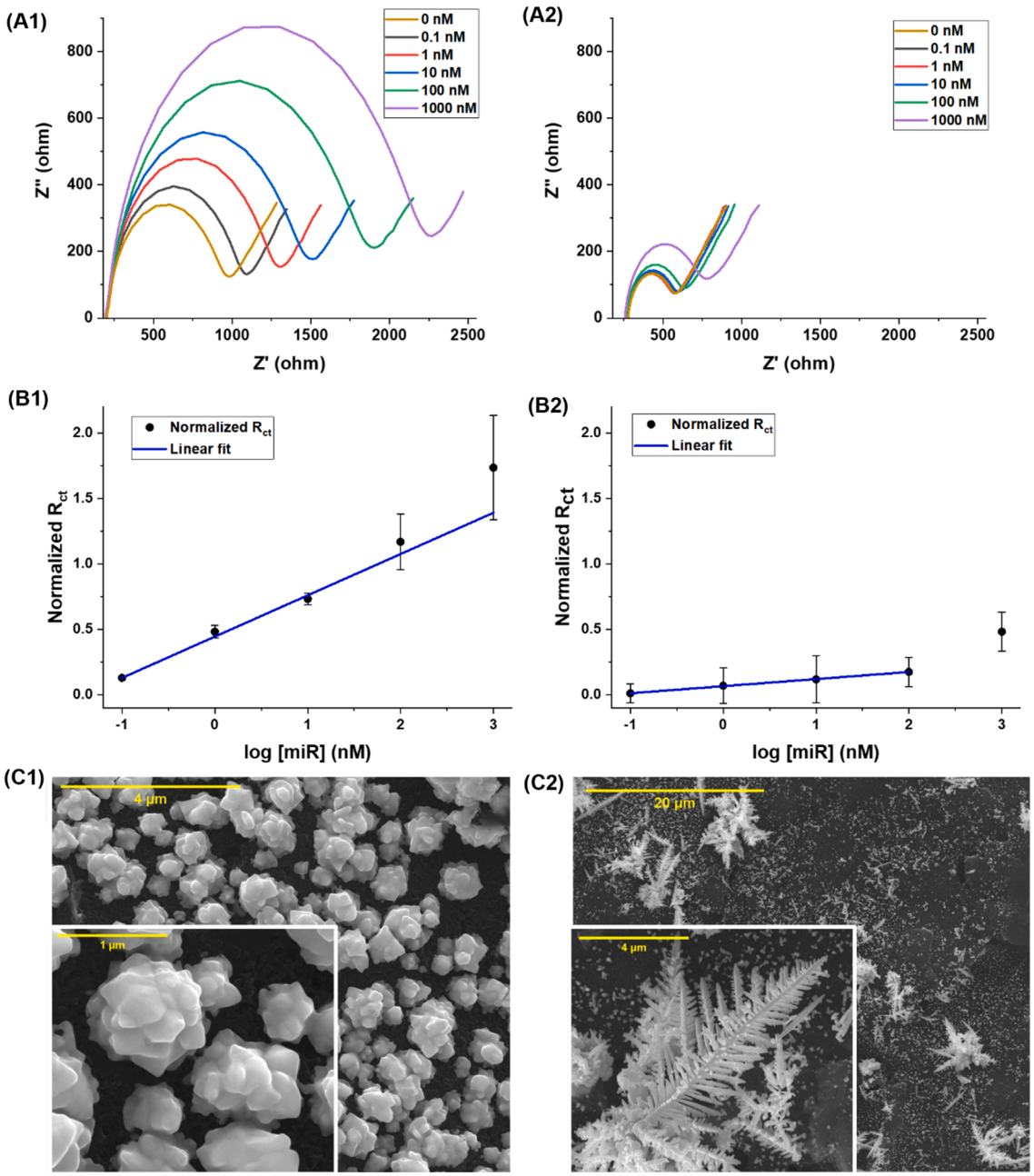

Fig. 3. Representative example of the (A) EIS analysis, (B) normalized R_{ct} calibration curves, and (C) SEM analysis obtained for the biosensors modified with (1) star-like or (2) snowflake-like AuNPs. B1 has a regression equation of $y = (0.32 \pm 0.02)x + (0.44 \pm 0.02)$ and a coefficient of determination (R^2) of $R^2 = 0.99287$. B2 has a regression equation of $y = (0.0542 \pm 0.0009)x + (0.065 \pm 0.001)$ and an $R^2 = 0.99945$. Calibrations performed with miR-34a (0.1 nM – 1000 nM) in hybridization buffer. Electrochemical measurements performed in 5 mM $[Fe(CN)_6]^{3-/4-}$ in phosphate buffer, pH = 7.4 The error bars in all calibration curves represent standard error. Fitting of all calibration curves was performed accounting for the standard error of the points.

calibration curve of the biosensors modified with star-like AuNPs has a slope of (0.32 ± 0.02) decades [miR, nM]$^{-1}$ and encompasses all five standards, whereas the calibration curve of the biosensors modified with snowflake-like AuNPs has a slope of (0.0542 ± 0.0009) decades [miR, nM]$^{-1}$ and only includes the four lowest standards. Considering that the slope is positively correlated to accuracy of the curves, the difference between slopes is again an indication that the snowflake-like AuNPs might be less favorable for hybridization. To understand this discrepancy, the surface of the two types of biosensors was characterized through SEM. The first conclusion to be taken from the images on Fig. 3**C** is that the AuNPs deposited by CV are much more evenly distributed and densely packed on the surface of the C-SPEs than the AuNPs deposited by CA. Thus, the surface area modified with the AuNPs deposited CV is higher, which could by itself justify the observed difference in hybridization performance. The second conclusion to take from Fig. 3**C** is that the AuNPs deposited by CV have an almost star-like shape whereas the ones deposited by CA have more of a snowflake-like structure. Moreover, the AuNPs deposited by CV are smaller and rounder than their counterparts, which could also enhance the performance difference observed. By providing a surface with a higher surface-to-volume ratio, the star-like nanostructures may allow the miRNA probes to sit further apart on the surface of the AuNPs, thus reducing the steric hindrance of hybridization [37] and promoting its occurrence.

Overall, accounting for the insights gathered from SEM and for the fact that the biosensors modified with star-like AuNPs produced a linear fit with a greater level of confidence and accuracy, this will be the

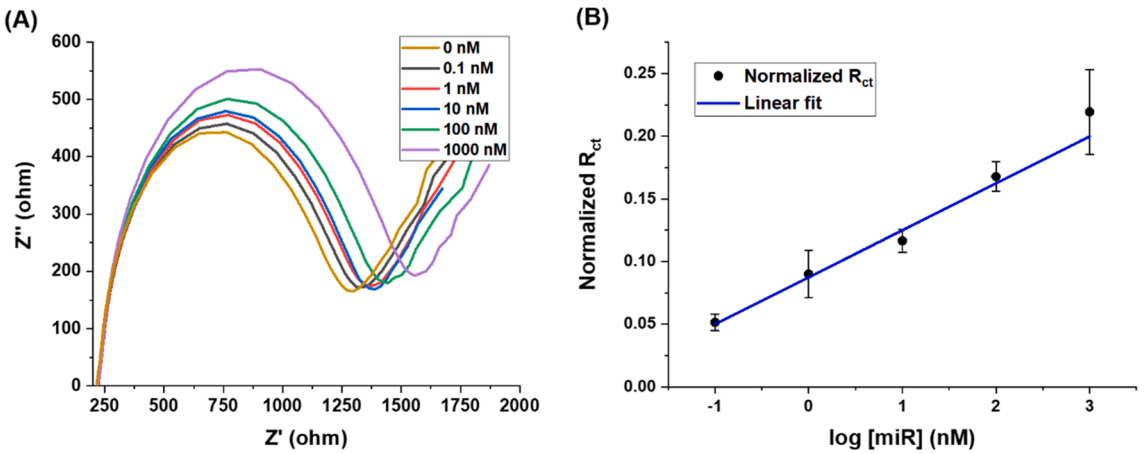

Fig. 4. Representative examples of the (A) EIS analysis and the (B) normalized R_{ct} calibration curve obtained for the calibration in the presence of serum, of the biosensors modified with star-like AuNPs. Calibration curve with a regression equation of y = (0.037 ± 0.003)x + (0.087 ± 0.003) and a coefficient of determination (R^2) of R^2 = 0.98555. Calibration performed with miR-34a (0.1 nM–1000 nM) in filtered and diluted FBS (1:100 in hybridization buffer). Electrochemical measurements performed in 5 mM $[Fe(CN)_6]^{3-/4-}$ in phosphate buffer, pH = 7.4.

morphology used in the remaining assays. It is noteworthy to mention that these biosensors have a linearity range (0.1–1000 nM) similar to other miR-34a biosensing platforms, and an LOD in phosphate buffer (39 pM) lower that some research work described in the literature for miR-34a detection[10,23,24,39].

3.3.2. Calibration curve in serum

The presence of miR-34a in systemic circulation and its association with AD have been previously demonstrated [9,11,20]. Therefore, commercial serum was used to obtain a more complex background matrix and to simulate the selectivity of the biosensor under real sample analysis conditions. For this purpose, the EIS response of the biosensor was evaluated using a series of miR-34a standards prepared in FBS. The EIS analysis represented in Fig. 4**A** shows that the diameter of the semicircles in the Nyquist plots increases with miR-34a concentration, i.e. that the R_{ct} of the biosensor is continuously increased by the binding of miR-34a to its sensory layer. However, this increasing trend is less noticeable than that observed when standards prepared in buffer are used. This difference can also be seen in the R_{ct} calibration curve in Fig. 4**B**; the R^2 is slightly lower and, most importantly, the slope is about 10-fold lower than the one of the calibration in buffer ((0.037 ± 0.003) decades [miR, nM]$^{-1}$ vs. (0.32 ± 0.01) decades [miR, nM]$^{-1}$, respectively). Nevertheless, the curve obtained for calibration in FBS is still accurate and reliable, and the decrease in slope can be justified by the increasing complexity of the medium. In the future, a filter with a smaller pore diameter could be used to try to filter out more interfering factors and improve the performance of the biosensor. Overall, the linearity range obtained for this calibration (0.1 nM to 1000 nM) was comparable, and the calculated LOD in serum (94 aM) was lower than that of other miR-34a biosensor platforms [10,23,24,39].

3.3.3. Specificity/ selectivity tests

To evaluate the specificity/selectivity of the biosensor, its response was studied in the presence of potentially interfering plasma substances: creatinine, miR-107 and commercial FBS 100-fold diluted. Both biomolecules have a low molecular weight, so they will be retained in solution after filtration. The results of these tests are summarized in **Fig. S.2** and show that the addition of either of these substances causes only a slight deviation in the biosensor's response (within the usual limits of acceptability). Thus, under the conditions tested, the biosensor demonstrated specificity/selectivity for miR-34a.

3.4. In vitro proof of concept

3.4.1. Neuronal differentiation

A human neuronal cell line (SH-SY5Y) commonly used in AD studies was selected to evaluate biosensor performance in a biologically relevant context. This cell line has a neuronal phenotype, which can be further differentiated by the addition of RA to the cell culture medium [42]. Furthermore, there is evidence that it may overexpress miR-34a in the cell culture media upon exposure to 6-OHDA [43]. To confirm neuronal differentiation with RA and to verify that the addition of 6-OHDA (50 or 100 μM) to the media elicited a significant response, the cells were observed under a brightfield microscope before fixation. **Figure S.3** contains representative images from each test condition (Non-DIFF, DIFF_0, DIFF_50, and DIFF_100), 5 days after plating. Focusing on neuronal differentiation, it can be seen that the DIFF cells exhibit a more pronounced spread-out morphology and a marked increase in neurite-like projections compared with the Non-DIFF cells, indicating differentiation of the SH-SY5Y cells into a more mature, neuron-like state [42] upon RA exposure. Moreover, the cell density 5 days after platting is similar across all conditions, which considering their different seeding densities, indicates that (i) the Non-DIFF cells proliferated at a different rate than the DIFF cells and (ii) the DIFF cells stopped proliferating, similarly to mature neuronal cells *in vivo* [44]. Taken together, there is strong evidence that the addition of RA to the medium induced neuronal differentiation.

Regarding the neurotoxic effect of 6-OHDA, the cell bodies of DIFF_100 cells appear to be smaller than those of DIFF_0 and DIFF _50 cells. Similarly, the DIFF_100 condition appears to have a higher proportion of round cells than its counterparts. Cytoplasmic condensation and cell rounding are two hallmarks of apoptosis [45] and indicate that the exposure to 6-OHDA may have induced cellular death. Furthermore, since the differences observed are more pronounced on the DIFF_100 than on the DIFF_50 condition, this apoptotic effect appears to be concentration dependent.

3.4.2. Immunocytochemistry

To better understand the effects of differentiation and exposure to 6-OHDA on the cells, they were subjected to immunocytochemical assays using β-tubulin III as a mature neuronal marker **(**Fig. 5**).** The staining of β-tubulin III was specific, as no green signal was detected in samples lacking the primary antibody (DIFF w/o 1st antibody). β-tubulin III can be detected under all conditions, including in non-differentiated cells. Although this marker is normally associated with mature neurons [42], undifferentiated SH-SY5Y cells have been reported to express both

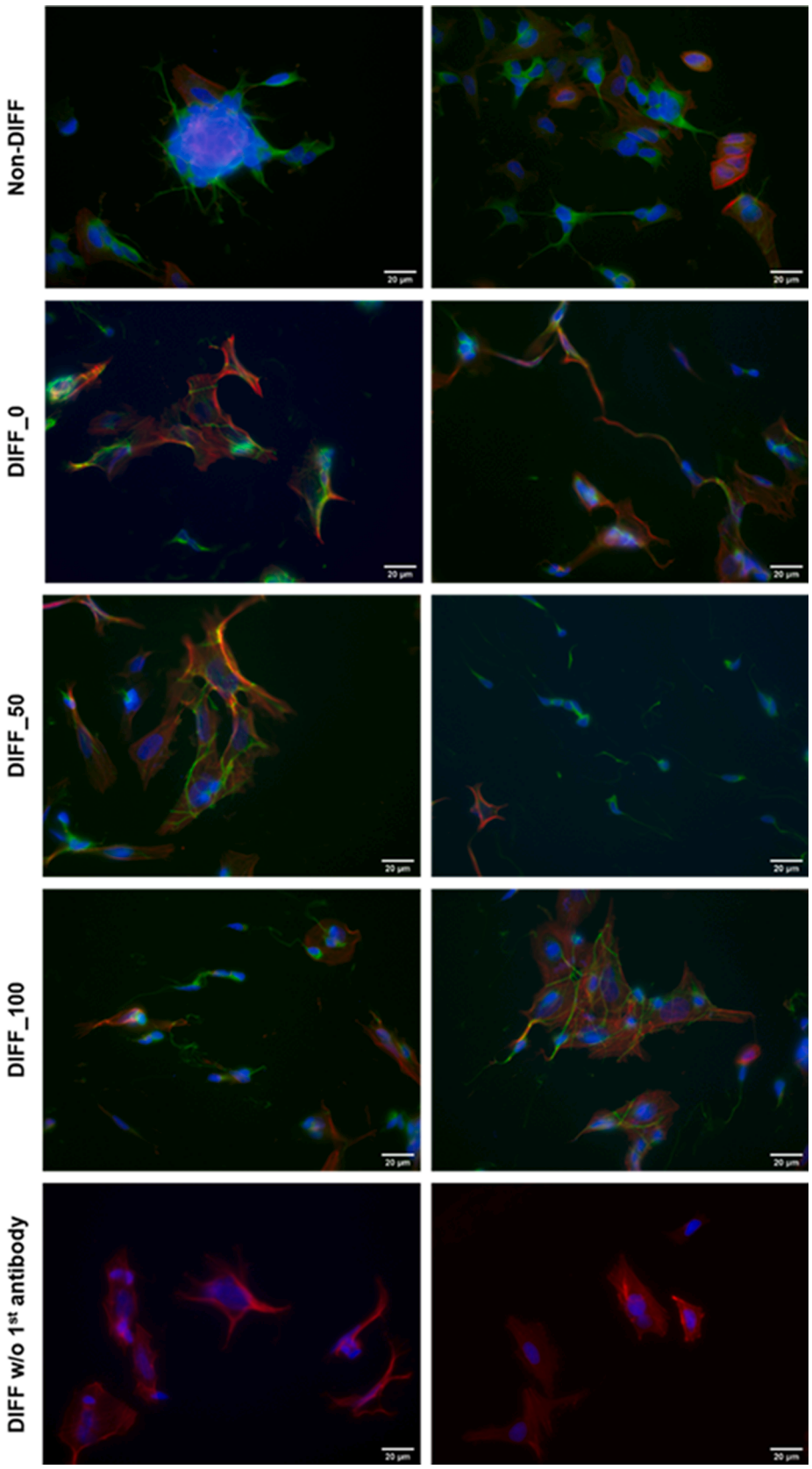

Fig. 5. Representative fluorescence images of the SH-SY5Y cells in undifferentiating (Non-DIFF) or differentiating conditions, in the presence of RA (DIFF_0) and 6-OHDA at 50 μM (DIFF_50) or 100 μM (DIFF_100). Green represents β-tubulin III, blue the nuclei and red F-actin. (For interpretation of the references to colour in this figure legend, the reader is referred to the web version of this article.)

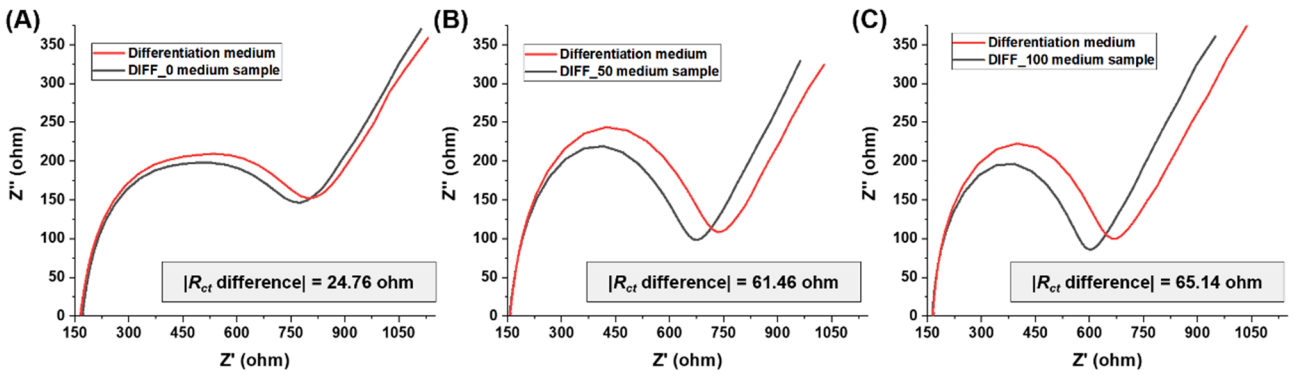

Fig. 6. EIS curves obtained for the incubation of cellular media extracts on the biosensors modified with star-like AuNPs. Stabilization performed in filtered and diluted Differentiation Medium (1:100 in hybridization buffer). Incubation performed in filtered and diluted samples (1:100 in hybridization buffer) of media used to culture (A) DIFF_0, (B) DIFF_50, or (C) DIFF_100 cells. Electrochemical measurements performed in 5 mM $[Fe(CN)_6]^{3-/4-}$ in phosphate buffer, pH = 7.4.

immature [46] and mature neuronal markers, including β-tubulin III [44,47]. Thus, this observation simply confirms the properties of the cell line used. Looking more closely at the expression of β-tubulin III, one can see that the spatial expression is non-equivalent among the conditions tested. In Non-DIFF cells, the β-tubulin III signal is more evenly distributed in the cell body, while in the DIFF cells, this signal is usually restricted to the periphery of the cells. This suggests a higher degree of microtubule organization within the cells exposed to RA (possibly associated with neurite formation), consistent with the bright-field observation that cells exposed to RA show a visible increase in neurite-like processes.

Another resemblance with the bright-field observations is the presence of similar cell densities in all conditions, even when seeding densities are different. In addition, cell clustering (a type of growth prevented by differentiation) was only observed on the Non-DIFF condition (Fig. 5, top, left). Again, this is an indication that exposure to RA stopped proliferation and allowed cells to spread and form neurites. In general, all images in Fig. 5 show cells with a differentiated morphology in simultaneous with cells with an undifferentiated morphology. Nevertheless, the relative proportion of differentiated cells is greater in wells treated with RA. This means that treatment with RA successfully resulted in differentiation, although some cells retained an undifferentiated morphology. Looking at the morphology of the nuclei, there is a clear difference in the cells exposed to 6-OHDA (DIFF_50 and DIFF_100 conditions); the nuclei appear to be more condensed and brighter. This may represent the observation of pyknotic nuclei, suggesting that cells underwent apoptotic nuclear condensation as a result of 6-OHDA exposure. Similar behaviors have been previously observed in bright-field images and described by others, including *Rehfeldt et al.* [48]. Analysis of phalloidin staining (red signal) shows that F-actin filaments appear to be more organized on DIFF conditions. This is consistent with all previous observations of RA-induced differentiation and is confirmation of its success. Overall, the fluorescence observations confirmed the bright-field observations: RA induced a neuronal-like phenotype on the SH-SY5Y cells and 6-OHDA appeared to have an apoptotic effect on these cells, although this can be better visualized in bright-field images.

3.5. Testing the sensor in cellular media extracts

To further validate the applicability of the biosensors, they were used to analyze cell culture media from differentiated SH-SY5Y cells with (DIFF_50 and DIFF_100) or without (DIFF_0) the 6-OHDA stimulus. Fig. 6 shows that addition of these samples to the biosensors caused a shift in R_{ct}, indicating that miR-34a was present in the cell medium. Upon closer inspection, this shift appears to be larger for the DIFF_50 sample than for the DIFF_0 sample, and even larger for the DIFF_100 sample, indicating that the concentration of miR-34a increases proportionally to the 6-OHDA concentration in the medium. This is an exciting result because it not only confirms the microscopic observations but also indicates that the stimulation of miR-34a excretion by 6-OHDA was successful and concentration-dependent. In the future, these results should be confirmed by an already well-established quantification technique, such as a TaqMan™ MicroRNA assay [49].

4. Conclusion

Here was demonstrated the successful development of an electrochemical miR-34a-based sensor for the diagnosis of AD. Regardless of the AuNPs used, the design was able to detect miR-34a in buffer. However, hybridization between the target and the probe was favored by star-shaped AuNPs (electrodeposited by CV) as opposed to snowflake-shaped AuNPs. With star-shaped AuNPs, the biosensor was also able to detect miR-34a in FBS, cell culture medium, and in the presence of potential interferents. Indeed, the biosensor was able to detect miR-34a within a linear range of 100 pM to 1 μM (in both buffer and serum), similarly to other miR-34a biosensors, while obtaining a lower LOD. In addition, this biosensor showed great potential for the analysis of cellular media extracts. Overall, this low-cost, sensitive, and selective biosensor provides an excellent basis for the development of a new AD diagnostic tool that will hopefully allow many patients to access early diagnosis and timely treatment.

Funding

This work was supported by 0624_2IQBIONEURO_6_E, 2IQBioneuro, Promotion of an R&I network in biological chemistry for the diagnosis and treatment of neurological diseases EP-INTERREG V Spain Portugal (POCTEP), and by Portuguese funds through FCT in the framework of the project PTDC/BTM-MAT/4156/2021. S.D.S acknowledges FCT (Fundação para a Ciência e a Tecnologia, I.P.) for her contract under the Norma Transitória–DL57/2016/CP/CP1360/CT0013.

Declaration of Competing Interest

The authors declare that they have no known competing financial interests or personal relationships that could have appeared to influence the work reported in this paper.

Data availability

The data that has been used is confidential.

Acknowledgments

The authors acknowledge Joana Guerreiro, PhD for the expert advice provided on oligonucleotide-based biosensors. The authors also acknowledge the support of the i3S Scientific Platform Bioimaging, member of the national infrastructure PPBI - Portuguese Platform of

Bioimaging (PPBI-POCI-01-0145-FEDER-022122) and to the projetct UID/EQU/04730/2020 - Center for Innovation in Engineering and Industrial Technology – CIETI.

Appendix A. Supplementary data

Supplementary data to this article can be found online at https://doi.org/10.1016/j.bioelechem.2023.108553.

References

[1] S. Absalon, D.M. Kochanek, V. Raghavan, A.M. Krichevsky, MiR-26b, upregulated in Alzheimer's disease, activates cell cycle entry, tau-phosphorylation, and apoptosis in postmitotic neurons, J. Neurosci. Off. J. Soc. Neurosci. 33 (37) (Sep. 2013) 14645–14659, https://doi.org/10.1523/JNEUROSCI.1327-13.2013.

[2] C.A. Lane, J. Hardy, J.M. Schott, Alzheimer's disease, Eur. J. Neurol. 25 (1) (Jan. 2018) 59–70, https://doi.org/10.1111/ene.13439.

[3] W. Wong, Economic burden of Alzheimer disease and managed care considerations, Am. J. Manag. Care 26 (8 Suppl) (Aug. 2020) S177–S183, https://doi.org/10.37765/ajmc.2020.88482.

[4] A. Villarejo Galende, M. Eimil Ortiz, S. Llamas Velasco, M. Llanero Luque, C. López de Silanes de Miguel, C. Prieto Jurczynska, Report by the Spanish Foundation of the Brain on the social impact of Alzheimer disease and other types of dementia, Neurología (English Edition) 36 (1) (2021) 39–49.

[5] S. Sarkar, S. Jun, S. Rellick, D.D. Quintana, J.Z. Cavendish, J.W. Simpkins, Expression of microRNA-34a in Alzheimer's disease brain targets genes linked to synaptic plasticity, energy metabolism, and resting state network activity, Brain Res. 1646 (Sep. 2016) 139–151, https://doi.org/10.1016/j.brainres.2016.05.026.

[6] S. Swarbrick, N. Wragg, S. Ghosh, A. Stolzing, Systematic review of miRNA as biomarkers in Alzheimer's disease, Mol. Neurobiol. 56 (9) (Sep. 2019) 6156–6167, https://doi.org/10.1007/s12035-019-1500-y.

[7] Z. Song, Y. Qu, Y. Xu, L. Zhang, L.i. Zhou, Y. Han, W. Zhao, P. Yu, Y.u. Zhang, X. Li, C. Qin, Microarray microRNA profiling of urinary exosomes in a 5XFAD mouse model of Alzheimer's disease, Anim. Models Exp. Med. 4 (3) (2021) 233–242.

[8] S. Gunes, Y. Aizawa, T. Sugashi, M. Sugimoto, P.P. Rodrigues, Biomarkers for Alzheimer's disease in the current state: a narrative review, Int. J. Mol. Sci., vol. 23, no. 9, Art. no. 9, Jan. 2022, doi: 10.3390/ijms23094962.

[9] Y. Zhao, Y. Zhang, L. Zhang, Y. Dong, H. Ji, L. Shen, The Potential Markers of Circulating microRNAs and long non-coding RNAs in Alzheimer's Disease, Aging Dis. 10 (6) (Dec. 2019) 1293–1301, https://doi.org/10.14336/AD.2018.1105.

[10] G. Congur, A. Erdem, PAMAM dendrimer modified screen printed electrodes for impedimetric detection of miRNA-34a, Microchem. J. 148 (Jul. 2019) 748–758, https://doi.org/10.1016/j.microc.2019.05.040.

[11] A. Nunomura, G. Perry, E. Izadpanah, RNA and Oxidative Stress in Alzheimer's Disease: Focus on microRNAs, Oxid. Med. Cell. Longev. 2020 (2020) 1–16.

[12] V.M. Serrano, I.S.P. Silva, A.R. Cardoso, M.G.F. Sales, Carbon electrodes with gold nanoparticles for the electrochemical detection of miRNA 21-5p, Chemosensors, vol. 10, no. 5, Art. no. 5, May 2022, doi: 10.3390/chemosensors10050189.

[13] P. Takousis, A. Sadlon, J. Schulz, I. Wohlers, V. Dobricic, L. Middleton, C.M. Lill, R. Perneczky, L. Bertram, Differential expression of microRNAs in Alzheimer's disease brain, blood, and cerebrospinal fluid, Alzheimers Dement. 15 (11) (2019) 1468–1477.

[14] M.M.J. van den Berg, J. Krauskopf, J.G. Ramaekers, J.C.S. Kleinjans, J. Prickaerts, J.J. Briedé, Circulating microRNAs as potential biomarkers for psychiatric and neurodegenerative disorders, Prog. Neurobiol. 185 (Feb. 2020), 101732, https://doi.org/10.1016/j.pneurobio.2019.101732.

[15] Y. Wu, Q. Li, R. Zhang, X. Dai, W. Chen, D. Xing, Circulating microRNAs: Biomarkers of disease, Clin. Chim. Acta 516 (May 2021) 46–54, https://doi.org/10.1016/j.cca.2021.01.008.

[16] D. Galimberti, C. Villa, C. Fenoglio, M. Serpente, L. Ghezzi, S.M.G. Cioffi, A. Arighi, G. Fumagalli, E. Scarpini, Circulating miRNAs as potential biomarkers in Alzheimer's disease, J. Alzheimers Dis. JAD 42 (4) (2014) 1261–1267.

[17] A. Turchinovich, L. Weiz, A. Langheinz, B. Burwinkel, Characterization of extracellular circulating microRNA, Nucleic Acids Res. 39 (16) (Sep. 2011) 7223–7233, https://doi.org/10.1093/nar/gkr254.

[18] C.E.L. Chua, B.L. Tang, miR-34a in Neurophysiology and Neuropathology, J. Mol. Neurosci. 67 (2) (Feb. 2019) 235–246, https://doi.org/10.1007/s12031-018-1231-y.

[19] P.K. Modi, S. Jaiswal, P. Sharma, Regulation of neuronal cell cycle and apoptosis by MicroRNA 34a, Mol. Cell. Biol. 36 (1) (Jan. 2016) 84–94, https://doi.org/10.1128/MCB.00589-15.

[20] J.P. Cogswell, J. Ward, I.A. Taylor, M. Waters, Y. Shi, B. Cannon, K. Kelnar, J. Kemppainen, D. Brown, C. Chen, R.K. Prinjha, J.C. Richardson, A.M. Saunders, A.D. Roses, C.A. Richards, Identification of miRNA changes in Alzheimer's disease brain and CSF yields putative biomarkers and insights into disease pathways, J. Alzheimers Dis. 14 (1) (2008) 27–41.

[21] C. Jian, M. Lu, Z. Zhang, L. Liu, X. Li, F. Huang, N. Xu, L. Qin, Q. Zhang, D. Zou, miR-34a knockout attenuates cognitive deficits in APP/PS1 mice through inhibition of the amyloidogenic processing of APP, Life Sci. 182 (2017) 104–111.

[22] X. Wang, P. Liu, H. Zhu, Y. Xu, C. Ma, X. Dai, L. Huang, Y. Liu, L. Zhang, C. Qin, miR-34a, a microRNA up-regulated in a double transgenic mouse model of Alzheimer's disease, inhibits bcl2 translation, Brain Res. Bull. 80 (4-5) (2009) 268–273.

[23] G. Congur, E. Eksin, A. Erdem, Impedimetric detection of microRNA at graphene oxide modified sensors, Electrochimica Acta 172 (2015) 20–27.

[24] E. Kesici, E. Eksin, A. Erdem, An impedimetric biosensor based on ionic liquid-modified graphite electrodes developed for microRNA-34a detection, Sensors, vol. 18, no. 9, Art. no. 9, Sep. 2018, doi: 10.3390/s18092868.

[25] S. Mohammadi-Yeganeh, M. Paryan, S. Mirab Samiee, M. Soleimani, E. Arefian, K. Azadmanesh, E. Mostafavi, R. Mahdian, M. Karimipoor, Development of a robust, low cost stem-loop real-time quantification PCR technique for miRNA expression analysis, Mol. Biol. Rep. 40 (5) (2013) 3665–3674.

[26] A.R. Cardoso, F.T.C. Moreira, R. Fernandes, M.G.F. Sales, Novel and simple electrochemical biosensor monitoring attomolar levels of miRNA-155 in breast cancer, Biosens. Bioelectron. 80 (Jun. 2016) 621–630, https://doi.org/10.1016/j.bios.2016.02.035.

[27] A. Blidar, O. Hosu, B. Feier, G. Ştefan, D. Bogdan, C. Cristea, Gold-based nanostructured platforms for oxytetracycline detection from milk by a 'signal-on' aptasensing approach, Food Chem. 371 (Mar. 2022), 131127, https://doi.org/10.1016/j.foodchem.2021.131127.

[28] M. Eduarda Schneider, L. Guillade, M.A. Correa-Duarte, F.T.C. Moreira, Development of a biosensor for phosphorylated Tau 181 protein detection in Early-Stage Alzheimer's disease, Bioelectrochemistry 145 (2022) 108057.

[29] A. Singh, A. Sharma, A. Ahmed, A.K. Sundramoorthy, H. Furukawa, S. Arya, A. Khosla, Recent advances in electrochemical biosensors: applications, challenges, and future scope, Biosensors 11 (9) (Sep. 2021) 336.

[30] G. Maduraiveeran, M. Sasidharan, V. Ganesan, Electrochemical sensor and biosensor platforms based on advanced nanomaterials for biological and biomedical applications, Biosens. Bioelectron. 103 (Apr. 2018) 113–129, https://doi.org/10.1016/j.bios.2017.12.031.

[31] G. Maduraiveeran, W. Jin, Nanomaterials based electrochemical sensor and biosensor platforms for environmental applications, Trends Environ. Anal. Chem. 13 (Jan. 2017) 10–23, https://doi.org/10.1016/j.teac.2017.02.001.

[32] S. Khizar, A. Elaissari, A.A. Al-Dossary, N. Zine, N. Jaffrezic-Renault, A. Errachid, Advancement in nanoparticle-based biosensors for point-of-care in vitro diagnostics, Curr. Top. Med. Chem. 22 (10) (2022) 807–833, https://doi.org/10.2174/1568026622666220401160121.

[33] M.-C. Daniel, D. Astruc, Gold nanoparticles: assembly, supramolecular chemistry, quantum-size-related properties, and applications toward biology, catalysis, and nanotechnology, Chem. Rev. 104 (1) (Jan. 2004) 293–346, https://doi.org/10.1021/cr030698+.

[34] X. Yu, Y. Jiao, Q. Chai, Applications of gold nanoparticles in biosensors, Nano LIFE 06 (02) (Jun. 2016) 1642001, https://doi.org/10.1142/S1793984416420010.

[35] M.A. Kader, N. Suhaity Azmi, A.K.M. Kafi, Recent advances in gold nanoparticles modified electrodes in electrochemical nonenzymatic sensing of chemical and biological compounds, Inorg. Chem. Commun. 153 (2023) 110767.

[36] K. Saha, S.S. Agasti, C. Kim, X. Li, V.M. Rotello, Gold nanoparticles in chemical and biological sensing, Chem. Rev. 112 (5) (May 2012) 2739–2779, https://doi.org/10.1021/cr2001178.

[37] H. Ravan, S. Kashanian, N. Sanadgol, A. Badoei-Dalfard, Z. Karami, Strategies for optimizing DNA hybridization on surfaces, Anal. Biochem. 444 (Jan. 2014) 41–46, https://doi.org/10.1016/j.ab.2013.09.032.

[38] J. Thangphatthanarungruang, C. Chotsuwan, S. Jampasa, W. Siangproh, A new nanocomposite-based screen-printed graphene electrode for sensitive and selective detection of 8-hydroxy-2′-deoxyguanosine, FlatChem 32 (Mar. 2022), 100335, https://doi.org/10.1016/j.flatc.2022.100335.

[39] J. Mandli, A. Amine, Impedimetric genosensor for miRNA-34a detection in cell lysates using polypyrrole, J. Solid State Electrochem. 22 (4) (Apr. 2018) 1007–1014, https://doi.org/10.1007/s10008-017-3819-5.

[40] W.-R. Zhao, T.-F. Kang, L.-P. Lu, F.-X. Shen, S.-Y. Cheng, A novel electrochemical sensor based on gold nanoparticles and molecularly imprinted polymer with binary functional monomers for sensitive detection of bisphenol A, J. Electroanal. Chem. 786 (Feb. 2017) 102–111, https://doi.org/10.1016/j.jelechem.2017.01.003.

[41] F.T.C. Moreira, M.G.F. Sale, M. Di Lorenzo, Towards timely Alzheimer diagnosis: A self-powered amperometric biosensor for the neurotransmitter acetylcholine, Biosens. Bioelectron. 87 (Jan. 2017) 607–614, https://doi.org/10.1016/j.bios.2016.08.104.

[42] R.F. Simões, R. Ferrão, M.R. Silva, S.L.C. Pinho, L. Ferreira, P.J. Oliveira, T. Cunha-Oliveira, Refinement of a differentiation protocol using neuroblastoma SH-SY5Y cells for use in neurotoxicology research, Food Chem. Toxicol. 149 (2021) 111967.

[43] Q. Ba, C. Cui, L. Wen, S. Feng, J. Zhou, K. Yang, Schisandrin B shows neuroprotective effect in 6-OHDA-induced Parkinson's disease via inhibiting the negative modulation of miR-34a on Nrf2 pathway, Biomed. Pharmacother. 75 (Oct. 2015) 165–172, https://doi.org/10.1016/j.biopha.2015.07.034.

[44] J.R. Murillo, L. Goto-Silva, A. Sánchez, F.C.S. Nogueira, G.B. Domont, M. Junqueira, Quantitative proteomic analysis identifies proteins and pathways related to neuronal development in differentiated SH-SY5Y neuroblastoma cells, EuPA Open Proteomics 16 (Sep. 2017) 1–11, https://doi.org/10.1016/j.euprot.2017.06.001.

[45] S. Ghavami, S. Shojaei, B. Yeganeh, S.R. Ande, J.R. Jangamreddy, M. Mehrpour, J. Christoffersson, W. Chaabane, A.R. Moghadam, H.H. Kashani, M. Hashemi, A. A. Owji, M.J. Łos, Autophagy and apoptosis dysfunction in neurodegenerative disorders, Prog. Neurobiol. 112 (2014) 24–49.

[46] S. Cetin, D. Knez, S. Gobec, J. Kos, A. Pišlar, Cell models for Alzheimer's and Parkinson's disease: At the interface of biology and drug discovery, Biomed. Pharmacother. 149 (May 2022), 112924, https://doi.org/10.1016/j.biopha.2022.112924.

[47] P. Tanapat, Neuronal Cell Markers, Mater. Methods, Jun. 2022, doi: //dx.doi.org/10.13070/mm.en.3.196.

[48] S.C.H. Rehfeldt et al., Neuroprotective Effect of Luteolin-7-O-Glucoside against 6-OHDA-Induced Damage in Undifferentiated and RA-Differentiated SH-SY5Y Cells, Int. J. Mol. Sci., vol. 23, no. 6, Art. no. 6, Jan. 2022, doi: 10.3390/ijms23062914.

[49] https://assets.fishersci.com/TFS-Assets/LSG/brochures/cms_042142.pdf.